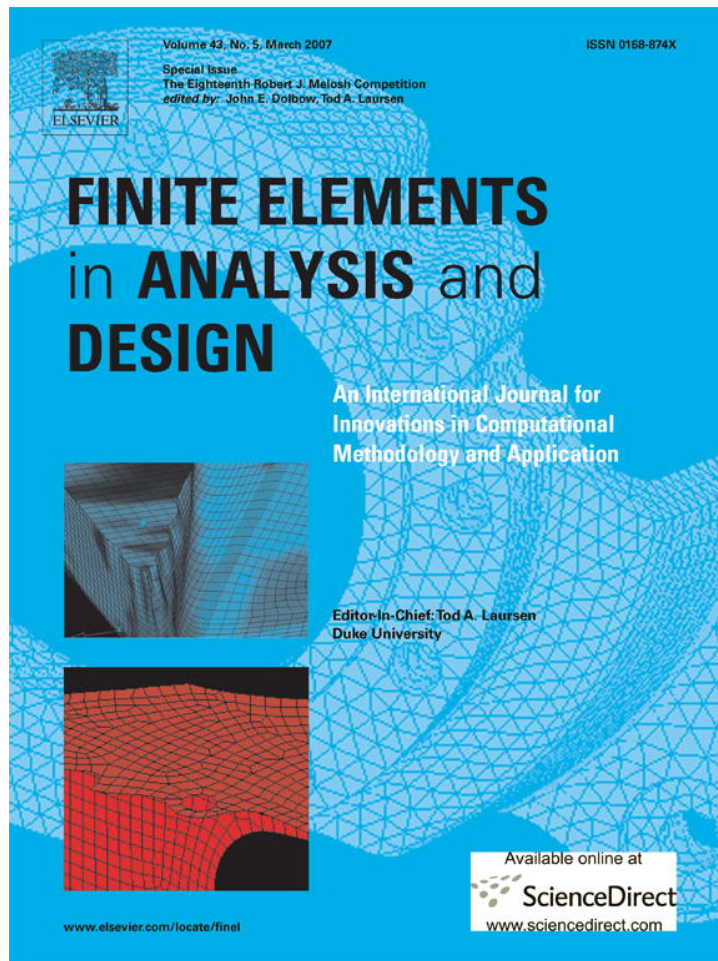


Provided for non-commercial research and educational use only.
Not for reproduction or distribution or commercial use.



This article was originally published in a journal published by Elsevier, and the attached copy is provided by Elsevier for the author's benefit and for the benefit of the author's institution, for non-commercial research and educational use including without limitation use in instruction at your institution, sending it to specific colleagues that you know, and providing a copy to your institution's administrator.

All other uses, reproduction and distribution, including without limitation commercial reprints, selling or licensing copies or access, or posting on open internet sites, your personal or institution's website or repository, are prohibited. For exceptions, permission may be sought for such use through Elsevier's permissions site at:

<http://www.elsevier.com/locate/permissionusematerial>



ELSEVIER

Available online at www.sciencedirect.com

ScienceDirect

Finite Elements in Analysis and Design 43 (2007) 384–396

FINITE ELEMENTS
IN ANALYSIS
AND DESIGN

www.elsevier.com/locate/finel

An atomic interaction-based continuum model for adhesive contact mechanics

Roger A. Sauer*, Shaofan Li

Department of Civil and Environmental Engineering, University of California, Berkeley, CA 94720, USA

Received 12 August 2006; accepted 30 November 2006

Available online 31 January 2007

Abstract

A micro/nano-scale computational contact mechanics model is proposed to study the adhesive contact between deformable bodies. To model adhesive contact, an interatomic interaction potential is incorporated into the framework of nonlinear continuum mechanics. The ensuing contact model is cast into an efficient finite element formulation which is implemented using an updated Lagrangian approach. The scaling of the model with respect to its geometrical size and the strength of adhesion is investigated. The proposed computational contact model is validated by a comparison with the analytical JKR and Maugis–Dugdale models.

© 2007 Elsevier B.V. All rights reserved.

Keywords: Adhesive contact; Computational contact mechanics; Continuum mechanics; Interatomic potential; JKR theory; Nano-mechanics; Scaling

1. Introduction

In this work we consider dry adhesive contact between small-scale, continuum bodies. The adhesive contact interaction between two bodies originates from the interaction of individual atoms belonging to the bodies. These interatomic interactions are characterized by weak, long range attraction and strong, short range repulsion. Adhesion is particularly strong if the bodies are highly compliant, so that a geometrically exact, large-deformation description should be considered.

The first adhesive contact model to appear is the widely used JKR theory by Johnson et al. [1]. The JKR model is an analytical model which extends the non-adhesive Hertzian contact theory (e.g see [2]). In the wake of the JKR model other theories followed, most prominently the DMT model by Derjaguin et al. [3] and the Maugis–Dugdale (M–D) model [4]. Although these models have been successfully applied to study rubber adhesion [1], MEMS stiction [5], adhesion of living cells [6], nanoindentation [7,8], atomic force microscopy [9] and the adhesion used by the Gecko [10], they have some major

limitations: They are restricted to infinitesimal deformations and special, e.g. spherical, geometry. To obtain more general models, the authors of [11,12] have considered finite element approaches to model adhesive contact. These approaches achieve to generalize the geometry and they have been successfully validated by the JKR and M–D models. However, in both [11,12] the interaction between the contacting bodies is not taken into account since one of the bodies is supposed to be rigid, thus decoupling the deformation between the two bodies in contact and simplifying the computational treatment substantially. In order to capture the interaction of largely deforming bodies during adhesive contact, a more general model is called for.

General large-deformation contact between deformable continua has been extensively studied by the field of computational contact mechanics [13,14]. Here, the research has been driven largely by the study of contact at the macroscale. From the macroscopic viewpoint contact is perceived as the impenetrability of two continua and is therefore usually modelled as a constrained optimization problem. Two bodies approaching each other do not interact as long as there is a gap in between. As the gap closes the impenetrability constraint becomes suddenly active. At the nanoscale, on the other hand, the transition is smooth and ranges from the weak attraction of bodies

* Corresponding author.

E-mail address: rogers@ce.berkeley.edu (R.A. Sauer).

well separated to the strong repulsion between bodies squeezed together. It is this smooth behavior and its atomic foundation which characterizes the interaction of nanoscale bodies. These mechanisms carry over to the macroscale as can be seen by the adhesion used by the Gecko [10,15]. On the toes of the Gecko millions of tiny spatula-shaped hairs, nanoscale in dimension, interact with an underlying surface leading to very strong adhesive forces and enabling the animal to cling to very rough or smooth surfaces.

In view of existing approaches, the objective therefore arises to incorporate the interatomic interaction occurring between two deformable bodies into a computational, large-deformation, continuum mechanical framework to study dry adhesive contact for small scales. At such scales the interatomic interaction can lead to the strong coupling between large regions of the bodies, so that from the numerical viewpoint it further becomes important to formulate efficient algorithms.

In [16] the present authors have proposed a large-deformation, continuum contact model based on interatomic interactions. These are homogenized, or coarse-grained, from the molecular dynamics description and the model is therefore termed the ‘Coarse-grained contact model’ (CGCM). In that work, the focus has been placed on the theoretical development of the model and its efficient implementation within a nonlinear finite element framework. The present paper serves to extend the previous work: The general behavior and scaling of the CGCM are further investigated and its application to adhesive contact mechanics is considered. In the following two sections we review the theory and FE implementation of the CGCM. Section 4 discusses its general behavior in dependence of two model parameters, which characterize the geometrical scale and the strength of adhesion. In Section 5 we validate the model by comparing it with the analytical M–D model. Conclusions are drawn in Section 6.

2. Continuum mechanical framework

In this section the proposed model, the CGCM, is formulated in the framework of large deformation continuum mechanics. We start by considering the interaction of two bodies as is illustrated in Fig. 1. The bodies are denoted by Ω_{10} and Ω_{20} in their reference configurations. Their current configurations are denoted by Ω_1 and Ω_2 . The deformation from one configuration to the other is described by the mappings φ_1 and φ_2 . Associated

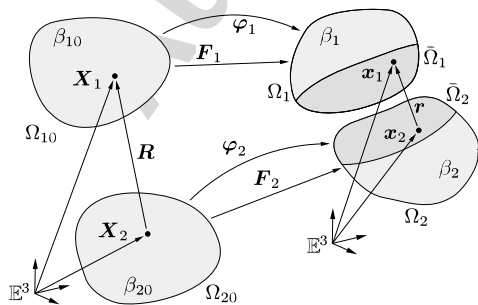


Fig. 1. Nanoscale continuum contact mechanics.

with these are the two deformation gradients $F_1 = \text{Grad } \varphi_1$ and $F_2 = \text{Grad } \varphi_2$, where the gradient operator is taken with respect to the reference configurations Ω_{10} and Ω_{20} . The bodies are subjected to the usual prescribed displacement and traction boundary conditions. The internal response of each body is considered as hyperelastic, i.e. it is described by the internal potential

$$\Pi_{\text{int}} = \int_{\Omega_0} W(\mathbf{F}) \, dV, \tag{1}$$

where $W(\mathbf{F})$ is the stored energy density in the reference configuration. It follows from the chosen constitutive relation modelling the material response. One such choice is the atomistic-based Cauchy–Born rule, which has been used to great extent in the literature, e.g. see [17] and references therein. The conjunction of the Cauchy–Born rule with the proposed CGC model has been studied in our earlier work [16]. Instead of the Cauchy–Born rule one can also consider a phenomenological energy density function W , like a Neo-Hookean or related model, e.g. see [18].

Returning to Fig. 1, we consider two generic points, denoted by $\mathbf{X}_1 \in \Omega_{10}$ and $\mathbf{X}_2 \in \Omega_{20}$ in the material domain and by $\mathbf{x}_1 \in \Omega_1$ and $\mathbf{x}_2 \in \Omega_2$ in the spatial domain. Further, the atomic or particle densities in the two respective configurations are denoted by β_{10} and β_{20} (in number of particles per reference volume), and β_1 and β_2 (in number of particles per current volume). The two descriptions are related by the Jacobian determinant of the mapping, as

$$\beta_0 = J\beta, \quad J = \det \mathbf{F}, \tag{2}$$

valid for both bodies. In view of the relation $dv = J \, dV$ between the volume differentials of the spatial and material configurations, it becomes apparent that the number of particles in a given volume is conserved, i.e. we have

$$\beta_0 \, dV = \beta \, dv = \text{const}. \tag{3}$$

This implies that, for now, we are not considering a flux of particles from, or into the bodies.

Within the CGC model the interaction between the two continua is modelled based upon the interaction of individual particles. For this, we consider that the interaction between two particles located at \mathbf{x}_1 and \mathbf{x}_2 , with distance $r = |\mathbf{x}_1 - \mathbf{x}_2|$, is modelled by a two point potential $\phi(r)$. In general $\phi(r)$ may be any potential applicable to the nature of the interaction between the particles; see for instance [19] for a comprehensive overview. A particular example is the van der Waals interaction, which is typically modelled by the Lennard-Jones potential

$$\phi(r) = \varepsilon \left(\frac{r_0}{r} \right)^{12} - 2\varepsilon \left(\frac{r_0}{r} \right)^6. \tag{4}$$

Here r_0 is the equilibrium distance where the force $F(r) = -\partial\phi(r)/\partial r$ vanishes, and ε corresponds to the energy well at $r = r_0$. Integration over all points \mathbf{x}_1 and \mathbf{x}_2 leads to the interaction energy

$$\Pi_C = \int_{\Omega_1} \int_{\Omega_2} \beta_1 \beta_2 \phi(r) \, dv_2 \, dv_1, \tag{5}$$

for the two interacting continua. Such a continuum approach dates back to the 1930s with the works of Bradley [20] and Hamaker [21], who have evaluated (5) for rigid spheres. In recent years the interaction energy Π_C has been considered in the numerical study of carbon nanotubes in the works of Arroyo et al. [22] and Qian et al. [23]. The novelty of our approach is the general setting within large deformation continuum mechanics and its efficient implementation into a numerical framework, such as the finite element method. It is noted that, due to a cutoff range of ϕ , the interaction can be restricted to the subdomains $\bar{\Omega}_1 \subseteq \Omega_1$ and $\bar{\Omega}_2 \subseteq \Omega_2$ shown in Fig. 1.

With the definition of the internal energy Π_{int} (1) of each body, their interaction energy Π_C (5), and the further presumption of the existence of an external energy Π_{ext} , the system shown in Fig. 1 becomes conservative and is governed by a variational principle. Its total potential energy is given by

$$\Pi = \sum_{I=1}^2 [\Pi_{\text{int},I} - \Pi_{\text{ext},I}] + \Pi_C, \quad (6)$$

where $I = 1, 2$ denotes the two bodies. Quasi-static equilibrium then follows from the principle of virtual work statement $\delta\Pi = 0$. The variation of the internal energy Π_{int} of each body can be written as

$$\delta\Pi_{\text{int}} = \int_{\Omega_0} \text{grad}(\delta\boldsymbol{\varphi}) : \boldsymbol{\sigma} \, dv, \quad (7)$$

where $\delta\boldsymbol{\varphi}$ denotes the variation of the motion, $\boldsymbol{\sigma}$ denotes the Cauchy stress field and the operator ‘:’ denotes the tensorial inner product. The external energy of each body is considered such that its variation can be expressed as

$$\delta\Pi_{\text{ext}} = \int_{\Omega} \delta\boldsymbol{\varphi} \cdot \bar{\mathbf{b}} \, dv + \int_{\Gamma_t} \delta\boldsymbol{\varphi} \cdot \bar{\mathbf{t}} \, da, \quad (8)$$

where $\bar{\mathbf{b}}$ and $\bar{\mathbf{t}}$ denote applied body forces and surface tractions. With the help of relation (3), the variation of the interaction energy Π_C becomes

$$\begin{aligned} \delta\Pi_C &= \int_{\Omega_1} \int_{\Omega_2} \beta_1 \beta_2 \left(\frac{\partial\phi}{\partial\mathbf{x}_1} \cdot \delta\boldsymbol{\varphi}_1 + \frac{\partial\phi}{\partial\mathbf{x}_2} \cdot \delta\boldsymbol{\varphi}_2 \right) \, dv_2 \, dv_1 \\ &= - \int_{\Omega_1} \delta\boldsymbol{\varphi}_1 \cdot \beta_1 \mathbf{b}_1 \, dv_1 - \int_{\Omega_2} \delta\boldsymbol{\varphi}_2 \cdot \beta_2 \mathbf{b}_2 \, dv_2, \end{aligned} \quad (9)$$

where we have identified the body forces

$$\begin{aligned} \mathbf{b}_1(\mathbf{x}_1) &:= -\frac{\partial\Phi_2}{\partial\mathbf{x}_1}, & \Phi_2(\mathbf{x}_1) &:= \int_{\Omega_2} \beta_2 \phi(r) \, dv_2, \\ \mathbf{b}_2(\mathbf{x}_2) &:= -\frac{\partial\Phi_1}{\partial\mathbf{x}_2}, & \Phi_1(\mathbf{x}_2) &:= \int_{\Omega_1} \beta_1 \phi(r) \, dv_1. \end{aligned} \quad (10)$$

This leads to the following physical interpretation: the mutual presence of the two continua leads to body forces acting on both bodies. The body force \mathbf{b}_1 acts at $\mathbf{x}_1 \in \Omega_1$ and depends on the current shape Ω_2 of body 2; the body force \mathbf{b}_2 acts at $\mathbf{x}_2 \in \Omega_2$ and depends on the configuration Ω_1 . Such is the continuum nature of this interaction. We note that the interaction is substantially simplified if one or both bodies are considered

rigid, such that the integration domains in Eq. (10) become fixed. This corresponds to the approach of infinitesimal continuum mechanics, where equilibrium is formulated on the undeformed configurations.

Collecting the term of Eqs. (7)–(9) above, the principle of stationary potential energy yields the weak form

$$\sum_{I=1}^2 \left[\int_{\Omega_I} \text{grad}(\delta\boldsymbol{\varphi}_I) : \boldsymbol{\sigma}_I \, dv_I - \delta\Pi_{\text{ext},I} - \int_{\Omega_I} \delta\boldsymbol{\varphi}_I \cdot \beta_I \mathbf{b}_I \, dv_I \right] = 0 \quad \forall \delta\boldsymbol{\varphi}_I, \quad (11)$$

governing the quasi-static two-body-interaction. We note that the derivation above can be extended to dynamic, impact-type problems by including the kinetic energy of the two bodies. For this we refer to our earlier work [16].

3. Efficient finite element implementation

The weak form (11) is implemented within the finite element method using an updated Lagrangian formulation, e.g. see [24]. For this, the displacement $\mathbf{u} = \mathbf{x} - \mathbf{X}$ and its variation $\delta\boldsymbol{\varphi}$ are approximated by the nodal sums

$$\begin{aligned} \mathbf{u}(\mathbf{x}) &\approx \sum_I^{n_{\text{no}}} N_I(\mathbf{x}) \mathbf{u}_I, \\ \delta\boldsymbol{\varphi}(\mathbf{x}) &\approx \sum_I^{n_{\text{no}}} N_I(\mathbf{x}) \mathbf{v}_I. \end{aligned} \quad (12)$$

Here n_{no} denotes the total number of finite element nodes of the two-body system, \mathbf{u}_I and \mathbf{v}_I denote the nodal values of fields \mathbf{u} and $\delta\boldsymbol{\varphi}$, and $N_I(\mathbf{x})$ denotes the finite element shape functions. In its discretized form, Eq. (11) is then written as

$$\mathbf{v}^T [\mathbf{f}_{\text{int}} + \mathbf{f}_C - \mathbf{f}_{\text{ext}}] = 0 \quad \forall \mathbf{v}, \quad (13)$$

where \mathbf{u} and \mathbf{v} are the stacked vectors of all nodal values \mathbf{u}_I and \mathbf{v}_I , and where \mathbf{f}_{int} , \mathbf{f}_C and \mathbf{f}_{ext} are force vectors acting at the finite element nodes. Eq. (13) holds for all variations \mathbf{v} so that equilibrium is given by the nonlinear equation

$$\mathbf{f} = \mathbf{f}_{\text{int}} + \mathbf{f}_C - \mathbf{f}_{\text{ext}} = 0, \quad (14)$$

which we assemble from the element level and solve using the Newton–Raphson method. We emphasize that the internal and external contributions \mathbf{f}_{int} and \mathbf{f}_{ext} are in the same form as they are usually treated in continuum mechanics. For instance, in the updated Lagrangian formulation, the elemental contribution to the internal forces is given as

$$\mathbf{f}_{\text{int}}^e = \int_{\Omega^e} \mathbf{B}_{\text{UL}}^T \boldsymbol{\sigma} \, dv, \quad (15)$$

where \mathbf{B}_{UL} is the strain–displacement matrix, e.g. see [25]. For the rest of this section, our attention is devoted to the novel contribution \mathbf{f}_C arising from the interaction potential Π_C (6). On the element level, the two-body interaction leads to the interaction of individual finite elements. Based on

expression (9) the interaction of an element $\Omega_i^e \in \Omega_1$ and an element $\Omega_j^e \in \Omega_2$ expresses itself by the two contributions (no sum on indices!)

$$\begin{aligned} \mathbf{f}_{C,i} &= \int_{\Omega_i^e} \int_{\Omega_j^e} \mathbf{N}_i^T \beta_i \beta_j \frac{\partial \phi}{\partial \mathbf{x}_i} dv_j dv_i, \\ \mathbf{f}_{C,j} &= \int_{\Omega_i^e} \int_{\Omega_j^e} \mathbf{N}_j^T \beta_i \beta_j \frac{\partial \phi}{\partial \mathbf{x}_j} dv_j dv_i, \end{aligned} \quad (16)$$

where \mathbf{N}_i and \mathbf{N}_j are matrices containing the shape functions of the nodes of element Ω_i^e and Ω_j^e , and where β_i, β_j are the current densities at $\mathbf{x}_i \in \Omega_i^e$ and $\mathbf{x}_j \in \Omega_j^e$. In Eq. (16) $\mathbf{f}_{C,i}$ is the force acting on element Ω_i^e while $\mathbf{f}_{C,j}$ is the force acting on element Ω_j^e . We note that, due to a cutoff radius r_c of potential ϕ , beyond which the interaction becomes negligible, not all elements of the two bodies interact: Only elements pairs whose distance is below r_c interact. The formulation above has been implemented and studied in our previous work [16]. It is the most direct formulation following from Eq. (9) without introducing any further approximation apart from (12), which becomes arbitrarily accurate by refining the finite element mesh. In [16] we have illustrated that this formulation can become computationally costly. The reason for this is that, even when considering a cutoff radius r_c , any point \mathbf{x} of one body is influenced by a *volume* of the neighboring body, also termed the ‘influencing region’. We showed, that by introducing reasonable approximations on the evaluation of integral (9), the influencing region can be reduced to a surface area, which leads to a surface interaction method. Depending on the FE discretization, such a method becomes much more efficient while still giving excellent accuracy. At most, the region of influence can be reduced down to a point, which introduces further approximations but gives a highly efficient method. This strategy, denoted by Method 3 in [16], is outlined below. The idea of Method 3, the ‘point formulation’, is simple: instead of obtaining the body forces \mathbf{b}_1 and \mathbf{b}_2 , given in Eq. (10), by numerical integration over the deformed configurations Ω_1 and Ω_2 , we approximate these domains by simpler shapes, over which ϕ can be integrated analytically. In the following we will consider approximating each domain in Eq. (10) by a flat half-space with constant density β and consider ϕ to be given by the Lennard-Jones potential (4). This case is illustrated in Fig. 2. The body force acting at the generic point \mathbf{x}_k ($k = 1$ or 2) is given by

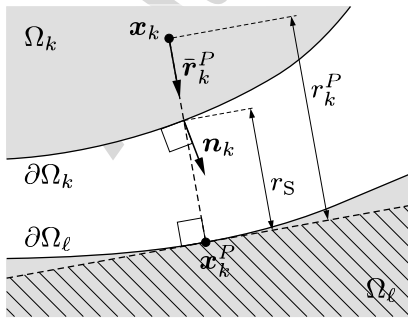


Fig. 2. Method 3: Closest point projection and approximation of Ω_ℓ by a flat half-space.

$\mathbf{b}_k = -\partial \Phi_\ell / \partial \mathbf{x}_k$ ($\ell = 2$ or 1) where the field Φ_ℓ follows by analytical integration as

$$\Phi_\ell := \int_{\Omega_\ell} \beta_\ell \phi dv_\ell = \pi \beta_\ell \epsilon r_0^3 \left[\frac{1}{45} \left(\frac{r_0}{r_k^P} \right)^9 - \frac{1}{3} \left(\frac{r_0}{r_k^P} \right)^3 \right]. \quad (17)$$

Here r_k^P denotes the distance between \mathbf{x}_k and the surface $\partial \Omega_\ell$. To evaluate (17) we need to determine the closest projection point \mathbf{x}_k^P , of point \mathbf{x}_k onto $\partial \Omega_\ell$, as is shown in the figure. Here we have defined

$$\mathbf{r}_k^P := \mathbf{x}_k^P - \mathbf{x}_k, \quad r_k^P := |\mathbf{r}_k^P|, \quad \bar{\mathbf{r}}_k^P := \frac{\mathbf{r}_k^P}{r_k^P}. \quad (18)$$

It is noted that this approximation becomes very accurate if the surface curvature and the density β of Ω_ℓ do not vary strongly within the cutoff radius r_c . Compared to the original formulation of Eq. (16), we can thus reduce the double volume integration to a single volume integration. As a further approximation we reduce the remaining volume integration over Ω_k to a surface integration over $\partial \Omega_k$ by writing $dv_k = \bar{\mathbf{r}}_k^P \cdot \mathbf{n}_k dr da_k$, according to Fig. 2, and integrate analytically along $\bar{\mathbf{r}}_k^P$, the direction of dr . This corresponds to projecting all body forces \mathbf{b}_k inside Ω_k and acting on the line along the direction $\bar{\mathbf{r}}_k^P$, i.e. which have the same projection point \mathbf{x}_k^P , onto the surface $\partial \Omega_k$. For this the body force \mathbf{b}_k is written as

$$\mathbf{b}_k(\mathbf{x}_k) = -\frac{\partial \Phi_\ell(r_k^P)}{\partial \mathbf{x}_k} = -\frac{\partial \Phi_\ell}{\partial r_k^P} \frac{\partial r_k^P}{\partial \mathbf{x}_k} = -F_\ell(r_k^P) \bar{\mathbf{r}}_k^P, \quad (19)$$

where we have $\partial r_k^P / \partial \mathbf{x}_k = -\bar{\mathbf{r}}_k^P$ and where the force $F_\ell := -\partial \Phi_\ell / \partial r_k^P$ follows readily from Eq. (17). The projection of all these forces acting along $\bar{\mathbf{r}}_k^P$ onto $\partial \Omega_k$ is then obtained by the integration

$$F_S(r_S) := \int_{r_S}^{\infty} F_\ell(r) dr = \Phi_\ell(r_S), \quad (20)$$

so that the nodal force vector acting on a surface element Γ_k^e discretizing $\partial \Omega_k$ is given by the surface integral

$$\mathbf{f}_{C,k} = \int_{\Gamma_k^e} \mathbf{N}_k^T \beta_k F_S(r_S) \bar{\mathbf{r}}_k^P \cos \alpha_k da_k. \quad (21)$$

Here \mathbf{N}_k is the matrix containing the shape functions of element Γ_k^e and we have defined $\cos \alpha_k := \bar{\mathbf{r}}_k^P \cdot \mathbf{n}_k$. We note that above the density β_k is assumed constant along dr , as it otherwise appears inside the integration of Eq. (20). It can be seen, that from the numerical point of view, Method 3 (21) is much more efficient to evaluate as the original formulation (16), since the double volume integration is replaced by a single surface integration. For this, we have approximated Ω_ℓ in the vicinity of \mathbf{x}_k^P by a flat half-space with constant density β_ℓ and assumed the density β_k of Ω_k to be constant along $\bar{\mathbf{r}}_k^P$. We further note that numerically, the projection point \mathbf{x}_k^P depends on the chosen surface discretization. The case of linear surface elements is described in further detail in [16].

In closing this section, we discuss how the approach presented above relates to some of the computational methods traditionally employed for contact mechanics problems, e.g. see [13,14]. Method 3 can be seen as a ‘Barrier Method’, where the barrier function is modelled upon an interatomic potential ϕ and thus captures some of the physical aspects of atomic interaction. Compared to common contact approaches like the Penalty, Lagrange Multiplier or Augmented Lagrangian methods, the proposed method presents some real advantages. First, the surface integral (21) can be evaluated for all surface elements regardless of their distance to the neighboring body, thus avoiding the distinction between active and inactive constraints needed for the traditional approaches mentioned above. Second, since the presented formulation is purely displacement based, one does not need to consider the LBB or inf-sup condition, characterizing numerical stability of mixed method approaches, e.g. see [26] and references therein. An important test to assess the accuracy of a given contact formulation is the contact patch test proposed by Taylor et al. [27] and later modified by Crisfield [28]. It can be verified that Method 3, proposed above, passes the patch test [29]. In summary, Method 3 avoids the LBB condition and passes the contact patch test. In [30] the authors argue that some of the existing contact algorithms, do not satisfy the LBB condition or the contact patch test.

4. General behavior of the CGC model

In this section we consider a simple axi-symmetric benchmark problem and study the general behavior of the contact model derived in Section 2. The study here confirms and extends our initial study of the plane strain example reported in [16]. The foremost attention here is placed on the scaling of the CGCM.

4.1. Benchmark problem

To illustrate the physical and numerical behavior we investigate the following model problem. Consider the axi-symmetric contact between a sphere with radius R_1 and a half-space ($R_2 = \infty$) as shown in Fig. 3. Both bodies are modelled by a nonlinear, hyperelastic (e.g. Neo-Hookean) constitutive model with constants $Y := E_1 = E_2$ and $\nu := \nu_1 = \nu_2$. The latter, which corresponds to Poisson’s ratio in the linear case, is fixed at $\nu = 0.2$. The parameter Y , which corresponds to Young’s

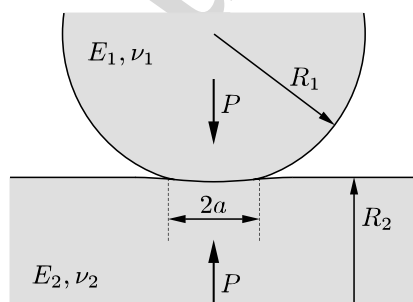


Fig. 3. Axi-symmetric contact between a sphere and half-space.

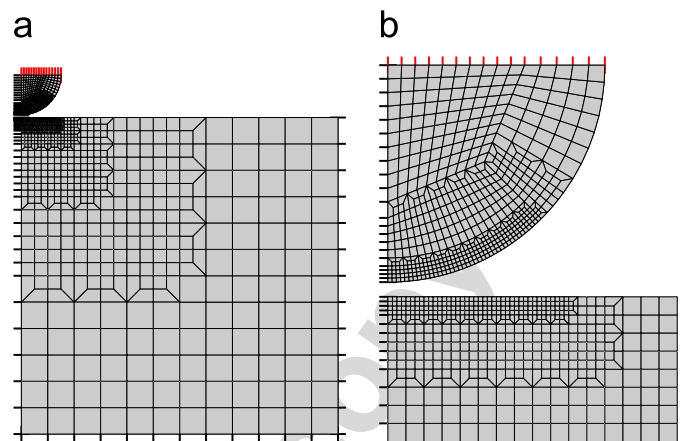


Fig. 4. Finite element discretization of the model problem: (a) Entire mesh; b. Zoom of the contact region.

modulus in the linear case, will be varied. The two bodies are pushed together by the relative approach u , which causes the resultant force P . We further suppose that $\beta_0 := \beta_{10} = \beta_{20}$. A finite element mesh used to compute the results of the CGC model is depicted in Fig. 4. It contains 1515 nodes and 1408 elements. It can be seen that the half-space is modelled by a block of size $8R_1 \times 8R_1$, which is sufficiently large to eliminate spurious boundary effects. The enlargement (b) shows the initial gap g between the tip of the sphere and the half-space beneath.

4.2. Normalization and scaling of the model problem

The quasi-static formulation of the CGC model can be fully normalized by selecting a reference length R_0 and a reference energy E_0 . We choose the radius of the sphere as our reference length, i.e. $R_0 = R_1$. It is an overall, macroscopic length scale. On the other hand, the interatomic equilibrium spacing r_0 of potential ϕ (4) represents an intrinsic, microscopic length scale. The ratio between these two length scales is defined by

$$\gamma_L := \frac{R_0}{r_0}. \quad (22)$$

It is a non-dimensional parameter describing the size of the considered problem. If $\gamma_L = \mathcal{O}(1)$ the geometry is of nanoscale proportions ($\sim 10^{-9}$ m and below) and contains only few interacting atoms; as γ_L increases the geometry becomes larger and larger, containing more and more atoms. (Values for $\gamma_L < \mathcal{O}(1)$ are not considered here, as the continuum modelling breaks down at some point.)

The reference energy E_0 is chosen based on the internal energy Π_{int} (1). As an example we consider a Neo-Hookean constitutive model with

$$W = U(J) + \frac{\mu}{2} (I_1 - 3) - \mu \ln J, \quad (23)$$

where $U(J) = A \ln(J)$ is the chosen volumetric response, where $J = \det \mathbf{F}$ and $I_1 = \text{tr}(\mathbf{F}^T \mathbf{F})$ characterize the deformation and

where A and μ are material constants, which are proportional to Y . In view of this proportionality we define

$$W_{\text{int},0} := Y, \quad (24)$$

as a *reference value of the internal energy density* W , and further, in view of Eq. (1) we define a *reference quantity of the internal energy* Π_{int} as

$$\Pi_{\text{int},0} := YR_0^3. \quad (25)$$

For a given deformation, i.e. constant W , the internal energy Π_{int} scales with the volume. This is reflected by $\Pi_{\text{int},0}$, which is also constant for progressing deformation. We choose $E_0 = \Pi_{\text{int},0}$ as the normalization parameter of the CGC model.

Similar to the internal energy density W , discussed above, we define the ‘interaction energy density’

$$W_C := c_0\beta_0\phi, \quad (26)$$

which is based on the interatomic interaction potential ϕ and the atomic density β_0 . Here c_0 is an arbitrary constant factor, which is introduced to adjust the formulation. In order to normalize the FE nodal force vector $\mathbf{f}_{C,k}$ (21) the choice $c_0 = \beta_0 r_0^3$, which is a material constant, is particularly convenient. The equilibrium energy of the potential ϕ is characterized by the material constant ε . With this in mind we further define the *reference quantity*

$$W_{C,0} := c_0\beta_0\varepsilon, \quad (27)$$

which is a material constant like $W_{\text{int},0}$. Associated with the density W_C is the interaction energy Π_C of the two solids Ω_1 and Ω_2 given by Eq. (5). Due to the rapid decay of ϕ , the energy Π_C only penetrates a distance proportional to r_0 into the solids and it therefore scales by $R_0^2 r_0$, i.e. from the macroscopic point of view (for large γ_L) it scales with the surface area R_0^2 of the bodies, whereas from the microscopic point of view ($\gamma_L = \mathcal{O}(1)$) it scales with the volume r_0^3 . Depending on the scale, Π_C is thus perceived as a surface energy or a bulk energy. In view of this scaling we define the *reference value of the interaction energy* Π_C as

$$\Pi_{C,0} := W_{C,0}R_0^2 r_0 = \beta_0^2 \varepsilon R_0^2 r_0^4. \quad (28)$$

Next, we define the ratio between the energy densities $W_{\text{int},0}$ and $W_{C,0}$ as

$$\gamma_W := \frac{W_{\text{int},0}}{W_{C,0}} = \frac{Y}{c_0\beta_0\varepsilon}, \quad (29)$$

which is a problem specific constant since Y , c_0 , β_0 and ε are treated as material constants. With γ_L (22) and γ_W we have defined two parameters which control the behavior of the considered model problem. The scaling of this problem, with respect to γ_L and γ_W is discussed in the following two sections. Before proceeding, let us comment on some consequences of the definitions above.

First, let us define the continuum energy ratio

$$\gamma_{\Pi} := \frac{\Pi_{\text{int},0}}{\Pi_{C,0}} = \gamma_L \gamma_W, \quad (30)$$

which increases linearly with the length scale γ_L , due to the fact that, from the macroscopic viewpoint, Π_{int} increases by the volume whereas Π_C increases with the surface area. Secondly, to assess stability one has to look at the stiffness. The deformation of the solids is of the order of R_0 , whereas the size of the gap changes by the order of r_0 . It thus follows that the stiffness associated with Π_{int} is characterized by the *reference quantity*

$$K_{\text{int},0} := \frac{\Pi_{\text{int},0}}{R_0^2} = YR_0, \quad (31)$$

which is proportional to the derivative $\partial^2 \Pi_{\text{int},0} / \partial R_0^2$, while the stiffness associated with Π_C is characterized by the *reference quantity*

$$K_{C,0} := \frac{\Pi_{C,0}}{r_0^2} = W_{C,0}R_0^2 / r_0, \quad (32)$$

which is proportional to the derivative $\partial^2 \Pi_{C,0} / \partial r_0^2$. Therefore the stiffness ratio between $K_{\text{int},0}$ and $K_{C,0}$ follows as

$$\gamma_K := \frac{K_{\text{int},0}}{K_{C,0}} = \frac{\gamma_W}{\gamma_L}, \quad (33)$$

which decreases for increasing length scales γ_L , due to the fact that, as γ_L increases, the intersolid, contact stiffness $K_{C,0}$ increases with respect to the internal, bulk stiffness $K_{\text{int},0}$. Several aspects of the behavior of the interacting two-body system can be explained by looking at either $K_{\text{int},0}$, $K_{C,0}$ or γ_K , as is discussed in later sections.

We summarize that we have defined two parameters, R_0 and E_0 , to normalize the CGC model, and two parameters, γ_L and γ_W to investigate the scaling of the model. The scaling, which is examined in the following two sections, is determined by relative changes in γ_L and γ_W , their magnitudes are arbitrary values, which follow from the previous definitions. In the remainder of this paper we use the equivalent parameters $\bar{\gamma}_L = \sqrt[3]{3/4}\gamma_L$ and $\bar{\gamma}_W = \sqrt{3}\gamma_W$.

4.3. Scaling of the geometry

This section illustrates how the CGC model behaves for various length scales γ_L . For this we consider the energy density ratio fixed at $\bar{\gamma}_W = 200$ and compare the behavior for the seven cases $\bar{\gamma}_L = 2, 5, 10, 20, 50, 100, 200$. Fig. 5 shows the dependence of the load $P(u)$ and gap $g(u)$ on the approach u as the two bodies come into contact. The seven curves displayed in both frames (a) and (b) correspond to the list of parameters $\bar{\gamma}_L$. The curves are computed with Method 3 using sufficiently small displacement increments Δu for the shown curves to appear smooth. The overall behavior of the load–displacement curve $P(u)$, shown in frame (a), and the gap–displacement curve $g(u)$, shown in frame (b) is characterized by three phases. We term the first phase the *rigid phase*, where the two bodies approach each other rigidly, without yet interacting. During this phase the force between the bodies and thus their deformation is zero; the gap decreases linearly. The second phase, termed

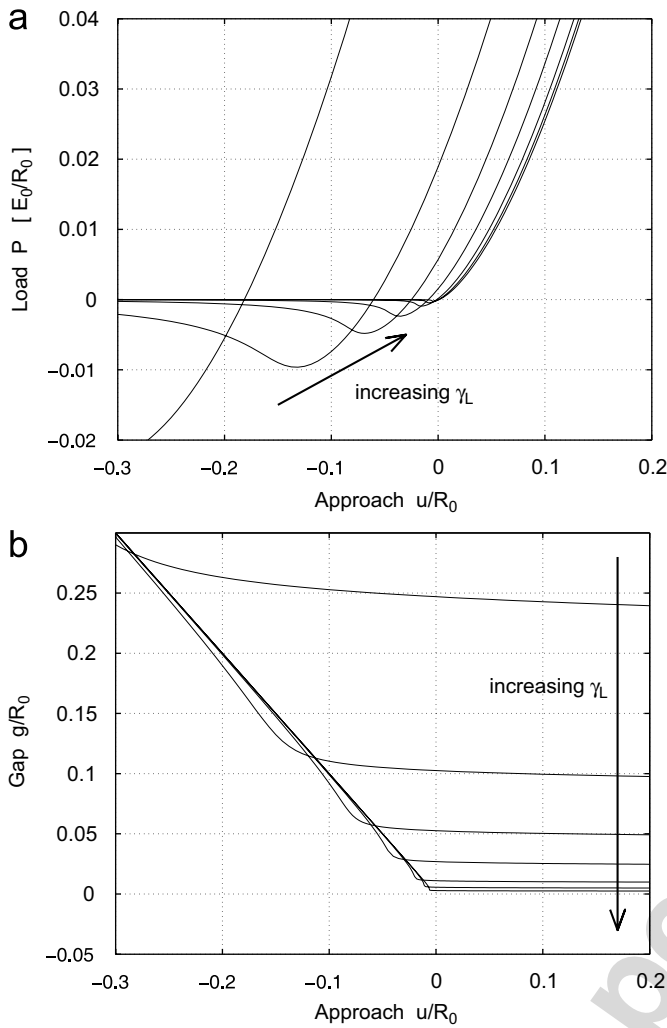


Fig. 5. (a) Load $P(u)$ and (b) Gap $g(u)$ in dependence of γ_L , for $\bar{\gamma}_W = 200$.

the *adhesion phase*, is characterized by an attractive (here negative) force P . During this phase the slope of $g(u)$ becomes steeper, i.e. the rate of change of the gap increases. The third phase is characterized by a large repulsive force P and only slight changes of the gap g . This last phase is termed the *contact phase*.

Fig. 5 shows the self-similarity of $P(u)$ and $g(u)$ across the geometrical scaling. In particular, as the length scale γ_L decreases, it can be observed that the gap and the minimum P_{\min} of $P(u)$ (i.e. where the adhesive attraction between the two bodies is strongest) decrease and attain their minima for larger displacements u . Further, frame (a) shows that, during the contact phase, i.e. for large positive P , the behavior of $P(u)$ is essentially unchanged for various γ_L : the curves all adopt the same stiffness as represented by the slope $P'(u)$ in Fig. 5. The reason for this behavior is that during the contact phase the increasing approach does not result in the decreasing of the gap but is rather accommodated by the deformation of the solids Ω_1 and Ω_2 , whose stiffness is characterized by $K_{\text{int},0}$ which is independent of γ_L . During the adhesion phase on the other hand

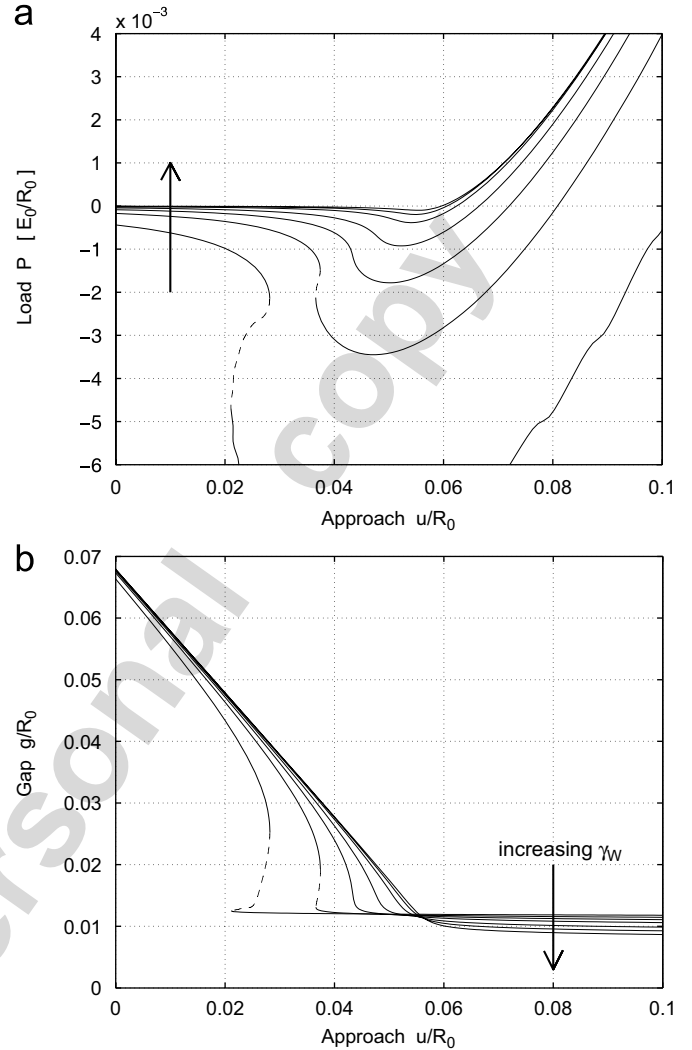


Fig. 6. (a) Load $P(u)$ and (b) Gap $g(u)$ in dependence of γ_W , for $\bar{\gamma}_L = 50$.

changes in the displacement are accommodated by changes of g (which are characterized by the γ_L dependent stiffness $K_{C,0}$), rather than by the deformation of the bodies.

In summary it is seen that γ_L determines the beginning of the adhesion phase, the magnitude of its extremum P_{\min} and the size of the contact gap. On the other hand, the slope $P'(u)$ during the contact phase is hardly affected by γ_L .

4.4. Scaling of the energy

In this section we assess the influence of the energy density ratio γ_W on the behavior of the load, stiffness and gap. For this we fix the length scale at $\bar{\gamma}_L = 50$ and consider the seven cases $\bar{\gamma}_W = 20, 50, 100, 200, 500, 1000, 2000$. Fig. 6 shows the behavior of $P(u)$ and $g(u)$ for the considered $\bar{\gamma}_W$. It can be observed that the maximum adhesion P_{\min} decreases as γ_W increases, whereas the contact stiffness and contact gap only depend slightly of γ_W . Furthermore, it can be observed, that below a threshold value of γ_W the adhesive approach turns unstable, as

occurs for the cases $\bar{\gamma}_W = 50$ and 20. For these cases the bodies are very soft compared to their mutual attraction. As the bodies approach each other the strength of attraction becomes so large that the stiffness of the two bodies is overwhelmed and they snap together suddenly. Likewise as one separates the bodies they will suddenly snap apart. In the literature, this behavior is often referred to as ‘jump-to-contact’ and ‘jump-off-contact’, e.g. see [31]. The unstable equilibrium path is marked as a dashed line in Fig. 6. The appearance of this physical instability can be explained by the parameter γ_K : As γ_K decreases (due to the decreasing of γ_W) the strength of adhesion, characterized by the stiffness $K_{C,0}$ increases with respect to the internal stiffness $K_{int,0}$.

Note that the load–displacement curve shown for $\bar{\gamma}_W = 20$, is not smooth but slightly oscillating. This is due to a discretizational error: for small γ_W the surface deformation becomes very large, due to the strong adhesion, such that further mesh refinement is needed to improve the results. The case $\bar{\gamma}_L = 50$, $\bar{\gamma} = 200$ and the case $\bar{\gamma}_L = 50$, $\bar{\gamma} = 20$ are further examined in the examples of the following section.

5. Comparison with analytical contact models

This section aims to validate the proposed CGCM. Therefore, the CGCM is compared with the prominent analytical theories developed for the contact of spherical bodies as shown in Fig. 3. We start by summarizing these theories in the section below; their relation and comparison with the CGCM follows in the preceding two sections.

5.1. The Maugis–Dugdale (M–D) model

The earliest contact model was obtained by Hertz in 1882, e.g. see [2]. His theory, however, does not account for adhesion between the contacting bodies. In the 1970s the Hertzian model was extended by the JKR [1] and DMT [3] theories to include adhesion. The JKR model applies to the limit case when $\gamma_W \rightarrow 0$, whereas the DMT model applies to the case $\gamma_W \rightarrow \infty$. In the 1990s Maugis [4] proposed a more general model valid for any γ_W and which contains the theories mentioned above as special cases. Since these models have been experimentally verified, e.g. see [1,9], they are used to validate the CGC model. The Hertzian, JKR, DMT and M–D models can be distinguished according to their predicted contact pressure distribution between the two contacting bodies. This is illustrated in Fig. 7. According to the Hertz and the DMT model the pressure distribution is elliptical and positive (i.e. compressive) throughout the contact zone. In case of the JKR model the contact pressure turns negative at the fringe of the contact zone. At $r = a$ the pressure is singular indicating a drawback of the JKR model. According to the M–D model the pressure extends beyond the contact zone, a , by taking a constant value within $a \leq r \leq ma$, where $m > 1$ is a parameter of this model.

In the following we outline the Hertz, JKR, DMT and M–D theories, e.g. see [4,32]. We start by defining the combined

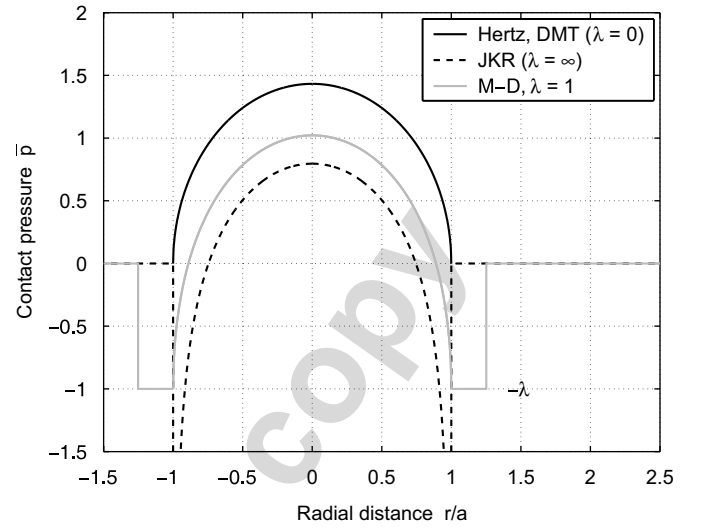


Fig. 7. Pressure Distribution between the contacting bodies.

elastic modulus

$$E := \left(\frac{1 - \nu_1^2}{E_1} + \frac{1 - \nu_2^2}{E_2} \right)^{-1}, \quad (34)$$

and the reduced radius

$$R := \left(\frac{1}{R_1} + \frac{1}{R_2} \right)^{-1}. \quad (35)$$

Further we consider the normalization of the force P , the contact radius a , the approach δ and the pressure p as

$$\begin{aligned} \bar{P} &:= \frac{P}{\pi w R}, & \bar{a}^3 &:= a^3 \frac{4E}{3\pi w R^2}, \\ \bar{\delta}^3 &:= \delta^3 \frac{16E^2}{9\pi^2 w^2 R}, & \bar{p}^3 &:= p^3 \frac{9R}{2\pi w E^2}, \end{aligned} \quad (36)$$

where w is the work of adhesion which is measured in units of energy per surface area. It is defined as the work required to separate two bodies adhering over a unit area from their equilibrium position to infinity, e.g. see [19]. It is similar to the surface energy, which is defined as the work necessary to increase the surface area of a body, and which can be viewed as the work required to separate two bonded (e.g. cohering) sections of the body. According to the Hertz theory we have

$$\bar{P}(\bar{a}) = \bar{a}^3, \quad \bar{\delta}(\bar{a}) = \bar{a}^2, \quad (37)$$

i.e. the force increases cubically, while the approach increases quadratically with increasing contact radius a . Combining these two expressions one arrives at the load displacement curve $\bar{P} = \bar{P}(\bar{\delta})$. By substituting (36) into (37) it can be confirmed that the work of adhesion w has no influence on the model. For the Hertz model the pressure distribution within the contact area is given by

$$\bar{p}(r) = \frac{3\bar{a}}{\pi} \sqrt{1 - \left(\frac{r}{\bar{a}}\right)^2} \quad \text{for } r \leq \bar{a}. \quad (38)$$

Outside the contact area, i.e. for $r > a$, the pressure is zero. For the JKR theory we have the two relations

$$\bar{P}(\bar{a}) = \bar{a}^3 - \sqrt{6\bar{a}^3}, \quad \bar{\delta}(\bar{a}) = \bar{a}^2 - \frac{2}{3}\sqrt{6\bar{a}}, \quad (39)$$

which depend on the work of adhesion since w does not cancel as it does for the Hertz formula. For the DMT model the corresponding relations between force P , approach δ and contact radius a are

$$\bar{P}(\bar{a}) = \bar{a}^3 - 2, \quad \bar{\delta}(\bar{a}) = \bar{a}^2, \quad (40)$$

which also depends on w . To present the M–D model we require the transition parameter

$$\lambda := \sigma_0 \sqrt[3]{\frac{9R}{2\pi w E^2}}. \quad (41)$$

It is dimensionless and corresponds to the normalization of σ_0 , which is the assumed constant value of the adhesive stress within $a \leq r \leq ma$. Letting $\lambda \rightarrow \infty$ yields the JKR model, while $\lambda \rightarrow 0$ gives the DMT model. Given λ and the contact radius \bar{a} one can solve the transcendental equation

$$\frac{\lambda \bar{a}^2}{2} \left(\sqrt{m^2 - 1} + (m^2 - 2) \arctan(\sqrt{m^2 - 1}) \right) + \frac{4\lambda^2 \bar{a}}{3} \left(\sqrt{m^2 - 1} \arctan(\sqrt{m^2 - 1}) - m + 1 \right) = 1, \quad (42)$$

for the parameter m . This parameter corresponds to the ratio of the Hertzian contact radius a and the contact radius ma of the M–D model, as is illustrated in Fig. 7. The JKR model is obtained from $m \rightarrow 1$ while $m \rightarrow \infty$ corresponds to the DMT model. For the M–D model the relation between force, approach and contact radius are, for a given λ ,

$$\bar{P}(\bar{a}) = \bar{a}^3 - \lambda \bar{a}^2 \left(\sqrt{m^2 - 1} + m^2 \arctan(\sqrt{m^2 - 1}) \right), \quad \bar{\delta}(\bar{a}) = \bar{a}^2 - \frac{4}{3} \lambda \bar{a} \sqrt{m^2 - 1}. \quad (43)$$

Further, for a given λ and \bar{a} the radial pressure distribution follows as

$$\bar{p}(r) = \frac{3\bar{a}}{\pi} \sqrt{1 - \left(\frac{r}{\bar{a}}\right)^2} - \frac{2\lambda}{\pi} \arctan \sqrt{\frac{m^2 - 1}{1 - \left(\frac{r}{\bar{a}}\right)^2}} \quad \text{for } r < a, \quad (44)$$

$$\bar{p}(r) = -\lambda \quad \text{for } a \leq r \leq ma.$$

The load-displacement curves $\bar{P} = \bar{P}(\bar{\delta})$, given implicitly by Eqs. (37), (39), (40) and (43) for the four models, are displayed in Fig. 8. It can be observed that for the Hertz model $\bar{P} \geq 0$, since no adhesion occurs. It can further be seen that the M–D model, depending on λ , poses a transition between the JKR and DMT model. The pressure distribution $\bar{p}(r)$ according to Eqs. (38) and (44) is displayed in Fig. 7.

We are further interested in the stress field inside the half-space due to the surface pressure $p(r)$. It can be obtained by integrating the known solution for a point load acting on a half-space. As an example, the stress component σ_z in the vertical

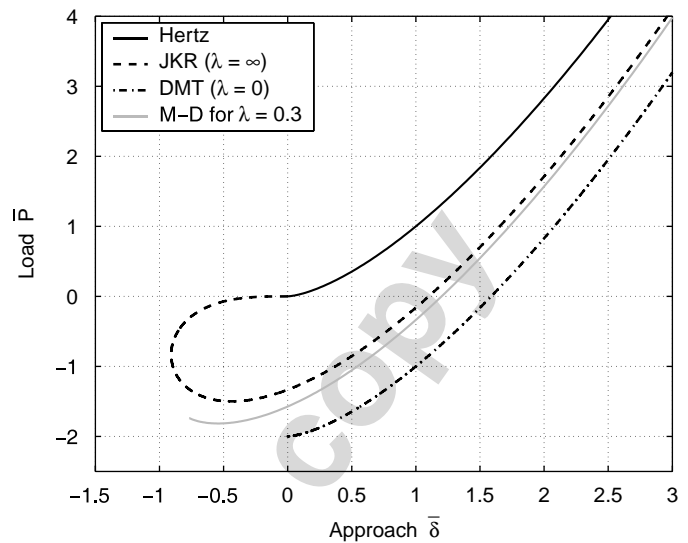


Fig. 8. Load–displacement curves $\bar{P}(\bar{\delta})$ for the Hertzian, JKR, DMT and M–D models.

z direction, due to a concentrated point load F at $r = 0, z = 0$, is given by

$$\sigma_z(r, z) = -\frac{3F}{2\pi} \frac{z^3}{\rho^5}, \quad (45)$$

where $\rho^2 := r^2 + z^2$, e.g. see [2,33]. The stress field has a singularity beneath the applied point load, which vanishes in the following integration. Integrating the stress field (45) for all point loads $F = p(s) dA$ yields

$$\sigma_z(r, z) = -\frac{3}{\pi} \int_0^c sp(s) \int_0^\pi \frac{z^3}{\rho^5} d\varphi ds, \quad (46)$$

where $\rho'^2 = r'^2 + z^2$ and $r'^2 = r^2 - 2rs \cos \varphi + s^2$ (see [29] for details). Due to the complexity of the integrand, Eq. (46) is evaluated numerically. It may be noted that at the surface ($z = 0$) we must have $\sigma_z(r, 0) = -p(r)$, so that we can avoid evaluating the integrand at the surface, where it turns singular.

5.2. Formal relation between the M–D and CGC models

In order to relate the two models we have to identify the work of adhesion w in the CGC model. Recall that w is defined as the work per unit surface area required to separate two adhering bodies from their equilibrium position to infinity. In Section 2 we derived the force F_S (20). It corresponds to the force exerted upon the surface element da_k of body Ω_k due to the presence of the neighboring body Ω_ℓ . The work of adhesion can thus be defined as

$$w := -\beta_k \int_{r_{S,0}}^\infty F_S(r) dr, \quad (47)$$

where $r_{S,0}$ is the equilibrium distance of the two neighboring bodies which follows from the condition $F_S = 0$ as $r_{S,0} = r_0/\sqrt[9]{15}$. It is sensible to consider the reference configuration

in Eq. (47) so that we use β_{10} and β_{20} instead of β_1 and β_2 in the definition above. Without this approximation the work of adhesion becomes dependent on the local deformation and we cannot associate w with a material constant anymore, as is usually considered. For the case $\beta_{10} = \beta_{20} = \beta_0$ Eq. (47) is evaluated as

$$w = f_w \beta_0^2 \epsilon r_0^4, \quad (48)$$

where we have introduced the abbreviation $f_w := (\pi/8)\sqrt[3]{15}$. In view of definition (28) we have the identity

$$w R_0^2 = f_w \Pi_{C,0}, \quad (49)$$

i.e. the interaction energy Π_C is proportional to the work of adhesion w multiplied by the area R_0^2 .

Further, we need to establish a link between the normalization of the CGC model, as discussed in Section 4.2, and the normalization of the M–D model defined by Eq. (36). For this we consider the specific problem displayed in Fig. 3 and particularized by $Y = E_1 = E_2$, $\nu = \nu_1 = \nu_2$, $R_1 = R_0$, $R_2 = \infty$ and $\beta_0 = \beta_{10} = \beta_{20}$. According to Eqs. (34) and (35) we thus have $E = f_E E_1$, $f_E := 1/2(1 - \nu_1^2)$ and $R = R_0$. As mentioned in Section 4.2 the CGCM is normalized by the parameters R_0 and $E_0 := \Pi_{\text{int},0}$ so that the normalization of a force F becomes $\bar{F}_C = R_0/E_0 F$, where the bar and subscript C are used to indicated the normalization scheme of the CGCM. The normalized force \bar{F}_{MD} , as used by the M–D and related models, is given by Eq. (36)₁. From Eqs. (49) and (30) it thus follows that

$$\bar{F}_C = f_F \bar{F}_{\text{MD}}, \quad f_F := \frac{\pi f_w}{\gamma_W \gamma_L}, \quad (50)$$

i.e. we have established the factor f_F relating the two normalization schemes. Likewise we treat the normalization of a length, given by $\bar{L}_C = L/R_0$ for the CGCM and given by Eqs. (36)₂ and (36)₃ for the contact radius a and approach δ within the M–D model. Now by using Eqs. (49), (30) and the definition of f_F we establish the relation between the normalization of the contact width

$$\bar{a}_C = f_a \bar{a}_{\text{MD}}, \quad f_a := \sqrt[3]{\frac{3}{4} f_F f_E}, \quad (51)$$

and the relation between the normalization of the approach

$$\bar{\delta}_C = f_\delta \bar{\delta}_{\text{MD}}, \quad f_\delta := f_a^2. \quad (52)$$

Finally, the relation between the stress normalization is obtained as

$$\bar{\sigma}_C = f_\sigma \bar{\sigma}_{\text{MD}}, \quad f_\sigma := \sqrt[3]{\frac{2}{9} f_F f_E^2}, \quad (53)$$

where $\bar{\sigma}_C = \sigma R_0^3/E_0$ is the stress normalization within the CGCM and where $\bar{\sigma}_{\text{MD}}$ is the stress normalization of the M–D model, given by Eq. (36)₄.

With Eqs. (50)–(53) we have established the formal relation between the two models, the analytical M–D model and the computational CGCM. It is noted that the M–D model only contains one free parameter, namely the transition parameter λ .

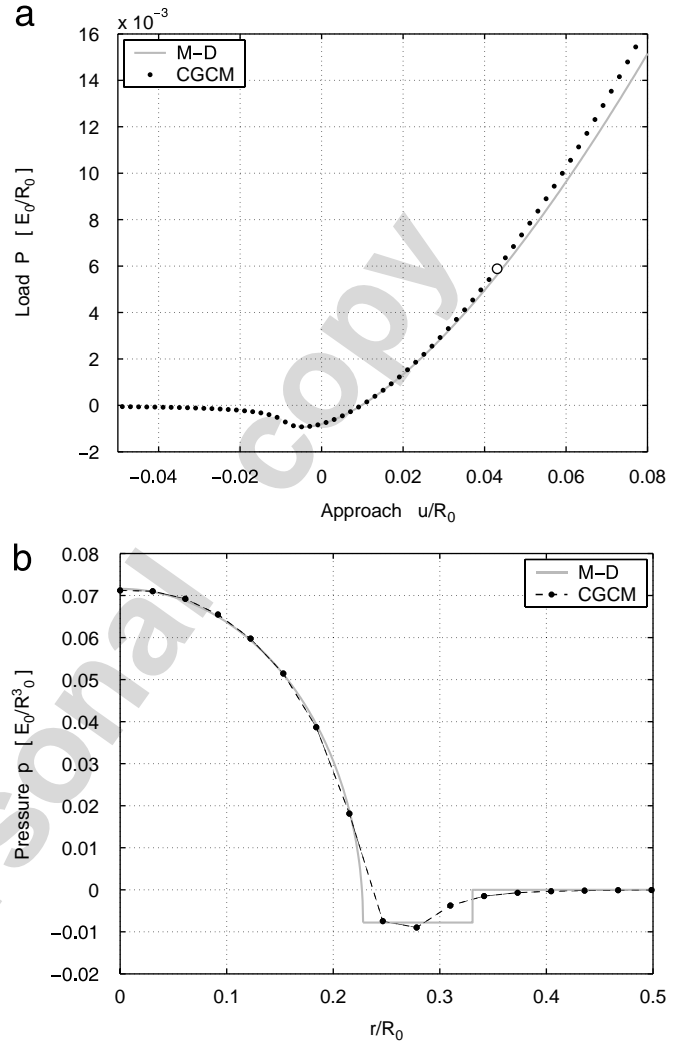


Fig. 9. Comparison for $\bar{\gamma}_L = 50$, $\bar{\gamma}_W = 200$: (a) Load-displacement curve; (b) Pressure distribution between sphere and half-space.

Physically it corresponds to a normalization of the peak attractive surface stress σ_0 , a quantity that may be difficult to assess experimentally. Further, the parameter λ is assumed fixed for a given material, a restriction which breaks down during the adhesion phase when the peak adhesion has not yet been attained. It can therefore not be expected that the M–D model is very accurate during this phase. The model is further restricted to infinitesimal deformations, so that we cannot expect the M–D model to perform well as the deformation becomes large.

The CGCM, on the other hand, is a large deformation model which accurately captures the long-range interaction during the adhesion phase. Fully normalized, it depends on two parameters, the length scale γ_L and the energy density ratio γ_W , which give the model greater flexibility in modelling adhesive contact. It is further emphasized that the CGCM is a model formulated for arbitrary geometry, whereas the M–D model applies only to particular cases like the spherical contact considered above.

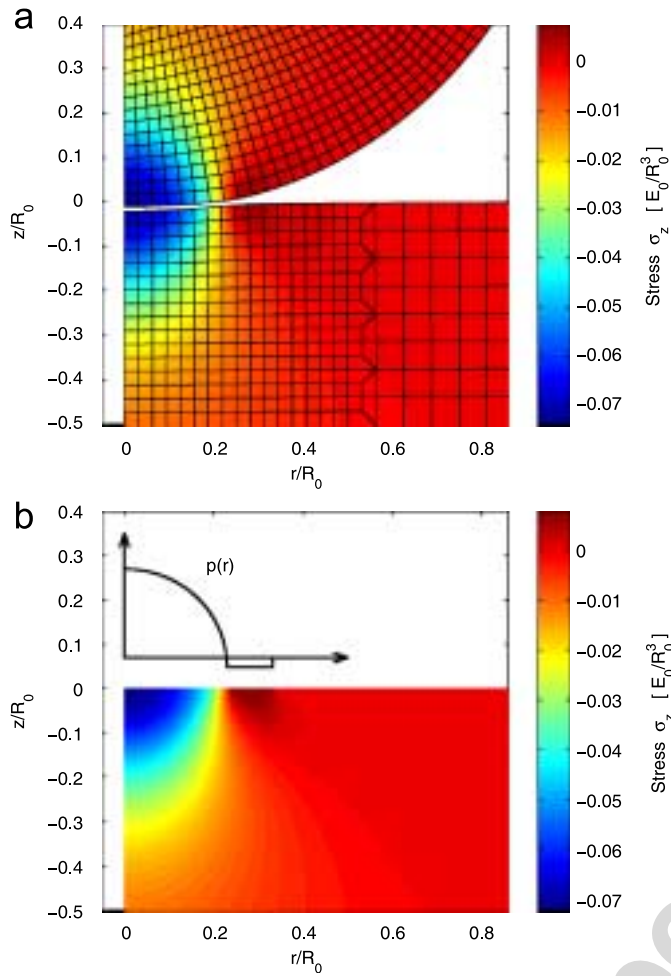


Fig. 10. Stress field σ_z for (a) the CGCM and (b) the M–D model, both for $\bar{\gamma}_L = 50$, $\bar{\gamma}_W = 200$.

5.3. Comparison between the M–D and CGC models

Let us now compare the behavior of the analytical M–D model, discussed above, and the CGCM. As a first example we pick the parameters $\bar{\gamma}_L = 50$ and $\bar{\gamma}_W = 200$. The results for this case are displayed in Figs. 9 and 10. Fig. 9(a) shows the load–displacement curve $P(u)$ of the computational and analytical models. The agreement is excellent over a wide range of displacements. As the approach grows large ($u \gg 0$) the M–D model loses its accuracy since the small deformation assumption is violated. As has been mentioned earlier the M–D model is not defined for large separations, so that for this situation ($u \ll 0$) only the computational CGCM result exists. As the bodies are pulled apart their interaction decays smoothly but, in principle, remains non-zero for arbitrary large distances, an effect which is failed to be captured by the M–D model.

Fig. 9(b) shows the normal pressure distribution $p(r)$ acting on the surface of the two opposing bodies. It is taken from the state $u \approx 0.043R_0$ and $P \approx 5.8 \times 10^{-3}E_0/R_0$, shown as an open circle on the $P(u)$ curve. This state corresponds to a contact radius of $a \approx 0.23R_0$ in the M–D model. In the

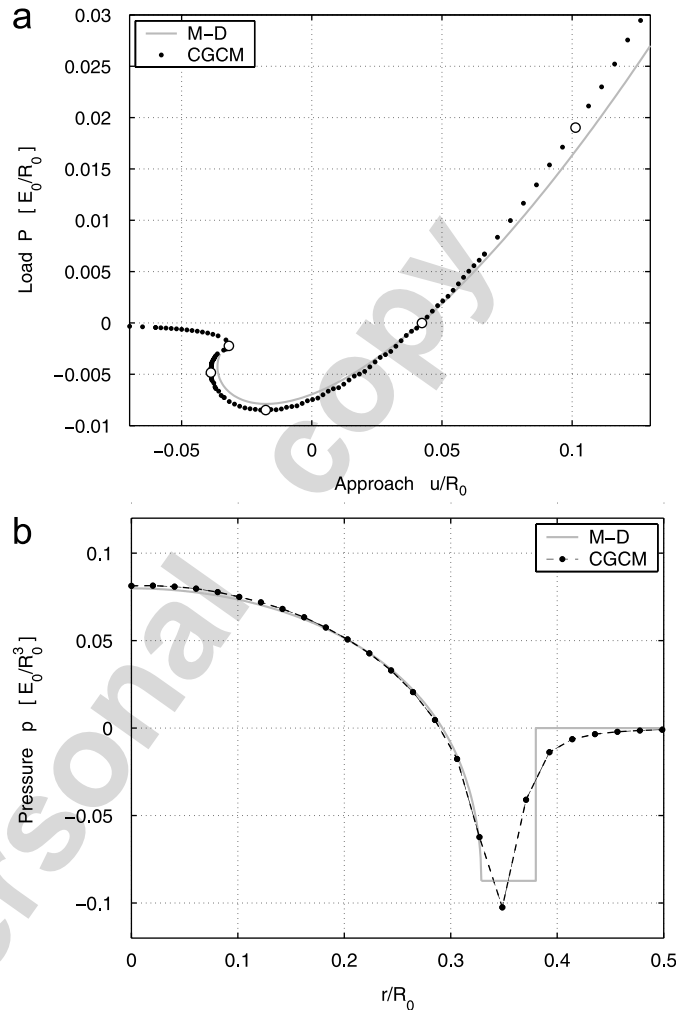


Fig. 11. Comparison for $\bar{\gamma}_L = 50$, $\bar{\gamma}_W = 20$: (a) Load–displacement curve; (b) Pressure distribution between sphere and half-space.

compressive ($p > 0$) regime we observe excellent agreement between the two models. In the tensile regime ($p < 0$), it is seen that the pressure distribution of the CGCM is continuous and decays smoothly to zero, whereas the pressure distribution of the M–D model is discontinuous and drops to zero abruptly. In all results presented on the first example, the parameter λ of the M–D model, which corresponds to the tensile stress level, is chosen on a best fit basis as $\lambda = 0.25$.

Fig. 10 shows the vertical stress component σ_z of the two models, which are in excellent agreement, even quantitatively. The same state $\{P, u\}$ as above is chosen. For the chosen parameters $\bar{\gamma}_L, \bar{\gamma}_W$ the tensile, adhesive stresses, which are present at the fringe of the contact zone, are small compared to the compressive stresses. The CGCM result is obtained from a finite element solution with the shown mesh, the M–D result is obtained from the numerical evaluation of Eq. (46).

As a second example we pick $\bar{\gamma}_L = 50$ and $\bar{\gamma}_W = 20$, a case where a physical instability exhibits itself during contact as has been discussed before in Section 4.4. The results for this case are displayed in Figs. 11 and 12. In Fig. 11(a) the

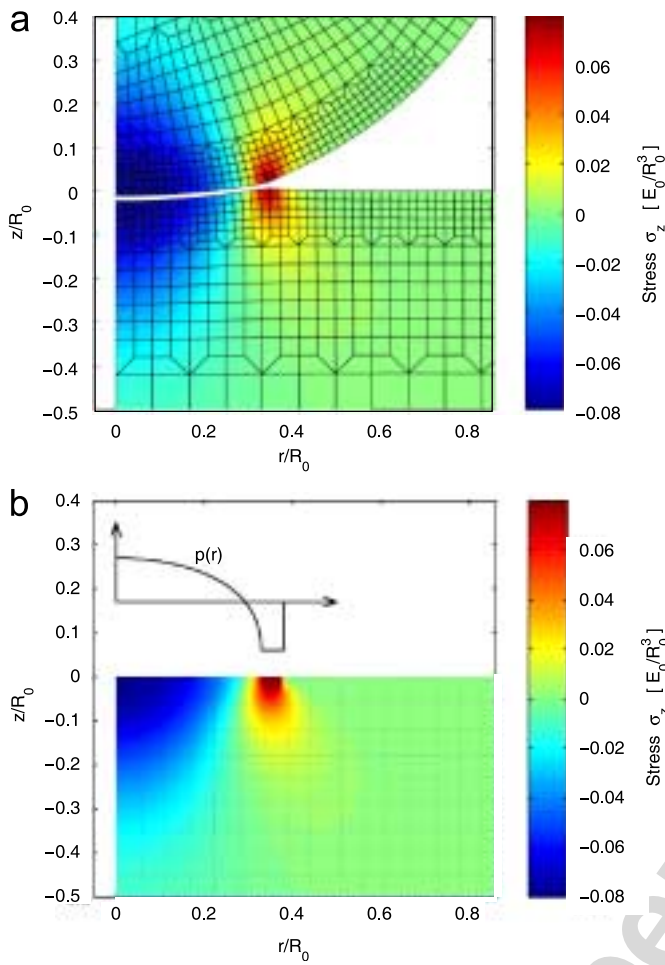


Fig. 12. Stress field σ_z for (a) the CGCM and (b) the M–D model, both for $\bar{\gamma}_L = 50$, $\bar{\gamma}_W = 20$.

load–displacement curves $P(u)$, as obtained by the two models, are compared. Their overall agreement is very good. The physical instability displays the characteristic looping behavior, where for a given displacement u we have three possible loads P . As has been remarked earlier the analytical contact theory cannot capture the adhesion phase accurately. Therefore differences between the analytical and computational results are inevitable. The path of $P(u)$, as obtained by the CGCM, is also supported by the numerical results reported in [34], which are based on infinitesimal theory. Fig. 11(b) shows the normal pressure distribution $p(r)$ acting on the surface of the two opposing bodies. Again we observe excellent agreement. Now, the adhesive pressure is much larger than for the first example. Its magnitude dominates over the compressive pressure. The pressure is taken at the state $u \approx 0.042R_0$ and $P \approx 0$, as corresponds to one of the states indicated by an open circle on the $P(u)$ curve. The M–D results are obtained for the choice $a \approx 0.33R_0$. Since $P = 0$ the vertical component of the shown pressure distribution integrates to zero. In all the results presented on the second example, the parameter λ of the M–D model is chosen on a best fit basis as $\lambda = 1.3$.

Fig. 12 shows the excellent agreement of the vertical stress component σ_z of the two models. Note the large local, adhe-

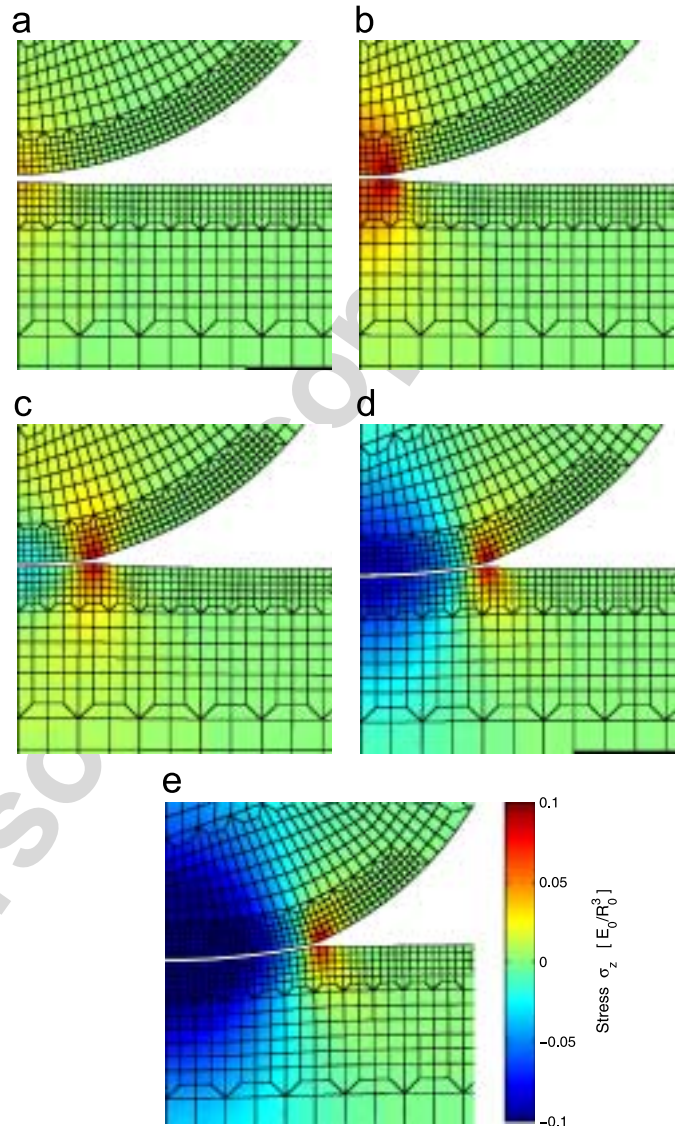


Fig. 13. Deformation and stress field σ_z during adhesive contact at the states shown as open circles in Fig. 11(a).

sive stress peak developing between the two contacting bodies. To capture this stress peak and the associated strong deformation a highly resolved FE mesh is needed, as is shown in frame (a). The stress distribution σ_z is computed at the same state $\{P, u\}$ considered for the pressure distribution above. It is noted that for $\bar{\gamma}_W = 20$ the bodies are so soft that their adhesion leads to a strong bulging deformation of the two opposing surfaces, as can be seen in frame (a). This follows from the fact that the stiffness ratio γ_K decreases along with γ_W . For low γ_W the behavior of the M–D comes very close to the behavior of the JKR model.

The evolution of the deformation and stress distribution σ_z of the two contacting bodies, as we trace the load–deformation curve, is shown in Fig. 13. The five displayed states correspond to the open circles shown on the load–displacement curve in Fig. 11(a). In particular, note that for the state in frame (d), the

net force acting between the two bodies is zero. For state (e) the net force is compressive, whereas for states (a), (b)–(c) the net force is tensile. The largest tension occurs at state (c).

6. Conclusions

In this work we have derived and studied a large-deformation, computational contact model which is based on interatomic interactions. These are homogenized, or coarse-grained by the integration approach of Eq. (5). The model is thus termed the coarse-grained contact model. The basic behavior of the interatomic interaction potential ϕ , i.e. the long range attraction and short range repulsion, carries over to the continuum model. In Section 3 we have presented an efficient finite element implementation of the model. Based on a simple benchmark problem, we have shown that the model only depends on two parameters, a length scale γ_L and a material constant γ_W . Their influence has been investigated and discussed. Finally, in the preceding section we have compared the CGC model with a widely used, analytical adhesive contact model, the Maugis–Dugdale model and its special case, the JKR model. The agreement is excellent, thus validating the proposed computational approach. In contrast to the mentioned analytical models, the CGCM is not restricted to spherical geometry and infinitesimal deformations: it is formulated for large deformation and general geometry. Further, the CGCM admits many possible extensions. Other potentials than the Lennard-Jones potential can be used, like for example electrostatic interaction. Secondly, the interaction can be restricted to the surface, e.g. modelling charged coated bodies, or it can be extended to multibody interaction; see [16]. Thirdly, the present FE implementation of Method 3 can be refined, e.g. by considering smoother surface discretizations. Fourthly, one can extend the model to the contact of plastic, viscous or frictional material behavior. An extension to dynamic, impact type problems will also be important. Finally, as γ_L becomes very large the present formulation tends to become ill-conditioned and should therefore be modified. A proposed modification is discussed in [29].

Acknowledgement

This work is supported by the NSF Grant No. CMS-0239130, which is greatly appreciated.

References

- [1] K.L. Johnson, K. Kendall, A.D. Roberts, Surface energy and the contact of elastic solids, *Proc. Roy. Soc. A*. 324 (1971) 301–313.
- [2] K.L. Johnson, *Contact Mechanics*, Cambridge University Press, Cambridge, 1985.
- [3] B.V. Derjaguin, V.M. Muller, Y.P. Toporov, Effect of contact deformation on the adhesion of particles, *J. Colloid Interface Sci.* 53 (2) (1975) 314–326.
- [4] D. Maugis, Adhesion of spheres: The JKR–DMT Transition using a dugdale model, *J. Colloid Interface Sci.* 150 (1) (1992) 243–269.
- [5] Y.-P. Zhao, L.S. Wang, T.X. Yu, Mechanics of adhesion in MEMS—a review, *J. Adhesion Sci. Technol.* 17 (4) (2003) 519–546.
- [6] Y.-S. Chu, S. Dufour, J.P. Thiery, E. Perez, F. Pincer, Johnson–Kendall–Roberts theory applied to living cells, *Phys. Rev. Lett.* 94 (2005) 028102.
- [7] A.C. Fischer-Cripps, *Nanoindentation*, second ed., Springer, New York, 2004.
- [8] Y.-P. Zhao, X. Shi, W.J. Li, Effect of work of adhesion on nanoindentation, *Rev. Adv. Mater. Sci.* 5 (2003) 348–353.
- [9] M.A. Lantz, S.J. O’Shea, M.E. Welland, Simultaneous force and conduction measurements in atomic force microscopy, *Phys. Rev. B* 56 (23) (1997) 15345–15352.
- [10] K. Autumn, et al., Evidence of van der Waals adhesion in gecko setae, *Proc. Natl. Acad. Sci. USA* 99 (19) (2002) 12252–12256.
- [11] A.Y. Suh, N. Yu, K.M. Lee, A.A. Polycarpou, H.T. Johnson, Crystallite coalescence during film growth based on improved contact mechanics adhesion models, *J. Appl. Phys.* 96 (3) (2004) 1348–1359.
- [12] S.-S. Cho, S. Park, Finite element modeling of adhesive contact using molecular potential, *Tribol. Int.* 37 (2004) 763–769.
- [13] P. Wriggers, *Computational Contact Mechanics*, Wiley, New York, 2002.
- [14] T.A. Laursen, *Computational Contact and Impact Mechanics: Fundamentals of Modelling Interfacial Phenomena in Nonlinear Finite Element Analysis*, Springer, Berlin, 2002.
- [15] K. Autumn, et al., Adhesive force of a single gecko foot-hair, *Nature* 405 (2000) 681–684.
- [16] R.A. Sauer, S. Li, A contact mechanics model for Quasi-Continua, *Int. J. Numer. Meth. Eng.*, 2007, in press.
- [17] R.E. Miller, E.B. Tadmor, The Quasicontinuum Method: Overview, applications and current directions, *J. Comp.-Aid. Mater. Des.* 9 (2002) 203–239.
- [18] R.W. Ogden, *Non-Linear Elastic Deformations*, Dover Ed., Mineola, 1997.
- [19] J.N. Israelachvili, *Intermolecular and Surface Forces*, second ed., Academic Press, London, 1991.
- [20] R.S. Bradley, The cohesive force between solid surfaces and the surface energy of solids, *Phil. Mag.* 13 (1932) 853–862.
- [21] H.C. Hamaker, The London–Van der Waals attraction between spherical particles, *Physica* 4 (10) (1937) 1058–1072.
- [22] M. Arroyo, T. Belytschko, Finite element methods for the non-linear mechanics of crystalline sheets and nanotubes, *Int. J. Numer. Meth. Eng.* 59 (2004) 419–456.
- [23] D. Qian, W.K. Liu, S. Subramoney, R.S. Ruoff, Effect of interlayer potential on mechanical deformation of multiwalled carbon nanotubes, *J. Nanosci. Nanotech.* 3 (1/2) (2003) 185–191.
- [24] T. Belytschko, W.K. Liu, B. Moran, *Nonlinear Finite Elements for Continua and Structures*, Wiley, Chichester, 2000.
- [25] K.-J. Bathe, *Finite Element Procedures*, Prentice-Hall, Englewood Cliffs, NJ, 1996.
- [26] K.-J. Bathe, The inf-sup condition and its evaluation for mixed finite element methods, *Comp. Struct.* 79 (2001) 243–252.
- [27] R.L. Taylor, P. Papadopoulos, On a patch test for contact problems in two dimensions, in: P. Wriggers, W. Wagner (Eds.), *Computational Methods in Nonlinear Mechanics*, Springer, Berlin, 1991, pp. 690–702.
- [28] M.A. Crisfield, Re-visiting the contact patch test, *Int. J. Numer. Meth. Eng.* 48 (2000) 435–449.
- [29] R.A. Sauer, An atomic interaction based continuum model for computational multiscale contact mechanics, Dissertation, University of California, Berkeley, 2006.
- [30] N. El-Abbasi, K.-J. Bathe, Stability and patch test performance of contact discretizations and a new solution algorithm, *Comp. Struct.* 79 (2001) 1473–1486.
- [31] B. Cappella, G. Dietler, Force–distance curves by atomic force microscopy, *Surf. Sci. Reports* 34 (1999) 1–104.
- [32] K.L. Johnson, J.A. Greenwood, An adhesion map for the contact of elastic spheres, *J. Colloid Interface Sci.* 192 (1997) 326–333.
- [33] S.P. Timoshenko, J.N. Goodier, *Theory of Elasticity*, third ed., McGraw-Hill, Singapore, 1970.
- [34] J.A. Greenwood, Adhesion of elastic spheres, *Proc. Roy. Soc. Lond. A* 453 (1997) 1277–1297.